J Seismol
https://doi.org/10.1007/s10950-021-10039-8

ORIGINAL ARTICLE

Brussels' bedrock paleorelief from borehole-controlled power laws linking polarised H/V resonance frequencies and sediment thickness

Koen Van Noten · Thomas Lecocq · Céline Goffin · Bruno Meyvis · Justine Molron · Timothy N. Debacker · Xavier Devleeschouwer

Received: 19 November 2020 / Accepted: 5 August 2021

Abstract The empirical power law relation (PR) between resonance frequency (f_0), obtained from H/V spectral ratio analysis of ambient noise, and sediment thickness (h), obtained from boreholes, is frequently used in microzonation studies to predict bedrock depth. In this study, we demonstrate (i) how to optimally construct a PR by including the error on the picked f_0 in the regression, and (ii) how to evaluate a regression quality by identifying the under- or overestimation of the sediment thickness prediction. We apply this methodology on f_0 data derived from 74 ambient noise recordings acquired above boreholes that reach the Brabant Massif bedrock below Brussels (Belgium). Separating the f_0 data into different subset based on the cover geology does not significantly improve the bedrock depth prediction because the cover geology in Brussels has common base layers. In Brussels, the PR relation $h = 88.631 f_0^{-1.683}$ is the best candidate to convert f_0 to depth, with a prediction error of 10%. The Brussels PR was subsequently applied on a local survey (404 measurements; 25 km^2) in southern Brussels with the aim to study Brussels' Brabant Massif bedrock paleorelief. By linking the obtained paleorelief, Bouguer gravity data and aeromagnetic data, a NNW-SSE oriented, 20 m-high subsurface ridge could be identified. This ridge stands out because of differential erosion between less-resistant and hard quartzitic rock formations of the Brabant Massif. This subsurface ridge deflects the local radiation of seismic energy resulting in an anomaly in the otherwise regional consistent azimuthal dependency of the resonance frequency. We conclude that adding a polarisation analysis to a microzonation survey analysis allows detecting anomalous features in the paleorelief.

Keywords H/V spectral ratio · Microzonation · Virtual Borehole · Polarisation · Brabant Massif

Supplementary Information The online version contains supplementary material available at https://doi.org/10.1007/s10950-021-10039-8.

K. Van Noten (✉) · T. Lecocq
Seismology-Gravimetry, Royal Observatory of Belgium, Ringlaan 3, 1180 Brussels, Belgium
e-mail: koen.vannoten@seismology.be

K. Van Noten · C. Goffin · B. Meyvis · X. Devleeschouwer
Geological Survey of Belgium, Royal Belgian Institute of Natural Sciences, Jennerstraat 13, 1000 Brussels, Belgium

J. Molron
Université Libre de Bruxelles, Avenue Franklin Roosevelt 50, 1050 Brussels, Belgium

J. Molron
Itasca Consultants S.A.S, 64 Chemin des Mouilles, 69130 Ecully, France

T. N. Debacker
TiBaScConsulting / Geognostics, Hofmeierstraat 7, 9000 Gent, Belgium

Published online: 27 January 2022

1 Introduction

Determining the sedimentary cover thickness above the seismic bedrock is an important parameter to tackle issues in seismic risk analysis and identifying the geothermal potential of the bedrock. In Belgium, the Netherlands, and the UK, the Meso-Cenozoic sediment thickness above the London-Brabant Massif (BM) partly controls (i) the damage distribution caused by large-magnitude earthquakes (Nguyen et al. 2004; García Moreno & Camelbeeck 2013) and (ii) the felt distribution of moderate-magnitude earthquakes (Hinzen 2005; Van Noten et al. 2015a, 2017). As both the sedimentary cover (Loveless et al. 2015) and the weathered top of the BM (Petitclerc et al. 2017) also have a geothermal potential, there is currently a strong renewed interest in mapping the paleo-relief of the top of the BM.

The 1-D Horizontal-to-Vertical Spectral Ratio (HVSR) analysis of ambient seismic noise is a widely applied non-invasive technique often used to determine the resonance frequency (f_0) of a site (Nogoshi & Igarashi 1970; Nakamura 1989). When the shear-wave velocity (*Vs*) contrast between soft sediments and the underlying bedrock is sufficiently large, HVSR analysis of ambient vibrations reveals this *Vs* impedance contrast, presuming that H/V ratio is dominated by the ellipticity of the fundamental mode of Rayleigh waves (Fäh et al. 2001). In regions of unknown subsurface, HVSR is hence a useful method to estimate the depth of the seismic bedrock (sensu Di Giulio et al. 2019). Converting f_0 to depth is, however, not a straightforward application. In areas with a uniform cover (1D, homogeneous horizontal layers) and a consistent bedrock depth, the mean Vs of the cover can be used to deduce the bedrock depth (h) according to generic formula (Roesset 1970):

$$h = \frac{Vs}{4.f_0} \tag{1}$$

However, if the cover and the subsurface geology are heterogeneous, the mean *Vs* of the cover varies laterally and Eq. 1 does not allow to calculate bedrock depth consistently in one region. Another approach to map bedrock depth was developed by Ibs-von Seht and Wohlenberg (1999) and Ibs-von Seht et al. (2008). These authors first determined f_0 from ambient vibration measurements above boreholes from which bedrock depth was known. Second, due to the non-linear increase of *Vs* with increasing bedrock depth, an empirical power law relation was defined according to the following generic equation:

$$h = a.f_0^b \tag{2}$$

with a and b defining the position and slope of the regression, respectively. a and b are linked to the local geology and geotechnical properties such as the soft sediment density, quality factor of sediments, compaction and *Vs*. By defining a and b by a best-fitting technique, any bedrock depth can be calculated at sites by performing new ambient vibration measurements (Delgado et al. 2002), without the necessity of applying a complex inversion, nor having knowledge on the mean *Vs* of the sedimentary cover. The disadvantage of using this method is that conditions in reality are slightly different than a perfect power law equation with low correlation coefficient (Ibs-von Seht & Wohlenberg 1999; Guéguen et al. 2007). Deriving a regression through a point cloud of measurements includes averaging the increasing *Vs* with depth while in reality lithological inhomogeneities and lateral velocity variabilities occur. Nevertheless these shortcomings, converting f_0 to depth using a regionally dependent power law has been used manifold for bedrock mapping (Ibs-von Seht & Wohlenberg 1999; Parolai et al. 2002; Hinzen et al. 2004; Dinesh et al. 2009; Benjumea et al. 2011; Poggi et al. 2012; Macau et al. 2015; Borges et al. 2016; Bignardi 2017; Mascandola et al. 2019; van Ginkel et al. 2020).

genericIn microzonation studies, the a and b power law parameters are often compared to investigate if parameters of other areas can be applied in the investigation area. This comparison results in a variability of different slopes in a log–log frequency-depth diagram but has often not much sense because each study area has its own geology, and hence its own velocity profile (Bignardi 2017), which leads to over- or underestimation of the bedrock depth (Thabet 2019; Benjumea et al. 2011). To account for this problem, Borges et al. (2016) were, to our knowledge, the first to separate a HVSR dataset into different power law equations. Although their separation was chosen arbitrary (with a separation criterion at 1 Hz based on the age of cover geology), such a separation should be applied more often because it may allow

defining higher data correlations while constructing the PR. Also Thabet (2019) computed different lithology-based power law relations because the seismometer data of the KiK-Net clearly exhibited different behaviours linked to the local geology.

In this study, we investigate if generating PRs for regions with a different cover geology improves the bedrock depth prediction compared to generating only one PR applicable for the entire region. Our criteria to separate the data set are based on the detailed knowledge of the tabular sedimentary cover geology of Brussels. We determined resonance frequency from 74 ambient noise measurements acquired above boreholes from which the BM bedrock depth is known. To choose the best candidate PR, we include the standard deviation on the picked f_0 to weight the regression and perform a regression quality control through a residual analysis of the predicted versus true bedrock depth. Afterwards, a HVSR dataset of 404 ambient noise measurements was acquired south of Brussels with the aim to reconstruct the bedrock paleorelief of the BM. The interpolated resonance frequency map is converted to depth using the best candidate PR and paleorelief results are linked to Bouguer anomaly and aeromagnetic maps. Complementary to the resonance frequency analysis, a HVSR polarisation analysis is performed to deduce the azimuthal direction in which f_0 has its maximum peak amplitude, which allows deducing anomalies in the paleorelief. While our regional paleorelief results improve the knowledge on the BM, the developed methodologies impact global microzonation efforts.

2 Geological setting and previous works

2.1 The Brabant Massif

The Brabant Massif (BM) is a strongly deformed, Lower Palaeozoic slate belt in subcrop in central and northern Belgium and in central UK. In Belgium, the BM is exposed along its southern rim along the flanks of incised river valleys filled with recent alluvial sediments (Quaternary). In Brussels, northern Belgium and southern Netherlands, chalk (Cretaceous), sands, silts and clays (Neogene/Paleogene), and loess (Quaternary) cover the BM. Borehole data indicates that the top of the BM dips to the north in Belgium and reaches a depth of 1000 m at the Belgian-Netherlands border (Legrand 1968). In this study, we focus on the southern rim of the BM where bedrock depth varies between a few metres and 150 m, respectively corresponding to a f_0 between 9 Hz and 0.68 Hz (Fig. 1). Nguyen et al. (2004) were the first in Belgium to link the dependency of f_0 with the sediment cover thickness above the BM (Fig. 1). A systematic decrease of f_0 is observed from a few Hz in river valleys at the southern rim of the BM (Molron 2015; Van Noten et al. 2015b) up to 0.22 Hz in the north near the border between Belgium and the Netherlands. In Flanders, a and b power law parameters are 90.439 and -1.27, respectively (Nguyen et al. 2004).

Below Brussels, the Brabant Massif forms the main competent contrast at depth. In the Campine Basin, however, Cretaceous, Carboniferous, and Devonian hard rock cover the BM. Here, HVSR analysis of ambient noise reveals several impedance contrasts and caution should be taken if one wants to use HVSR to map the BM bedrock depth in the Campine Basin (Fig. 1). Verbeeck (2019) demonstrated that in the Campine region, the base of the Cenozoic (base Hannut Formation; see further) can be considered as the seismic bedrock.

The general stratigraphy, structural grain and seismicity within the BM have been resolved in the past by filtering and interpreting (residual) Bouguer gravity and aeromagnetic potential field data (Chacksfield et al. 1993; Sintubin 1999; Debacker 2001; Piessens et al. 2004; Debacker et al. 2005; Matthijs et al. 2005; Van Noten et al. 2015a; Herbosch & Debacker 2018). Below Brussels, two Lower Palaeozoic formations are identified: the Lower Cambrian Tubize Formation (TUB), which consists of alternating quartzites and slates, and the Lower Cambrian Blanmont Formation (BLM), which predominantly consists of series of medium-grained quartzites. The paleorelief of the BM has been shaped by repetitive episodes of positive vertical movements since the Brabantian deformation and after the main erosive phase following the end of the Late Cretaceous-Early Cenozoic (Danian) flooding over the BM area. The resulting preserved erosional/weathered morphology of the top of the BM is dominated by differential erosion of the weathered and fractured sandstones/slates and quartzites composing the core of the concealed Anglo-Brabant deformation belt. Detecting and interpreting this differential erosional surface is the interest of this paper.

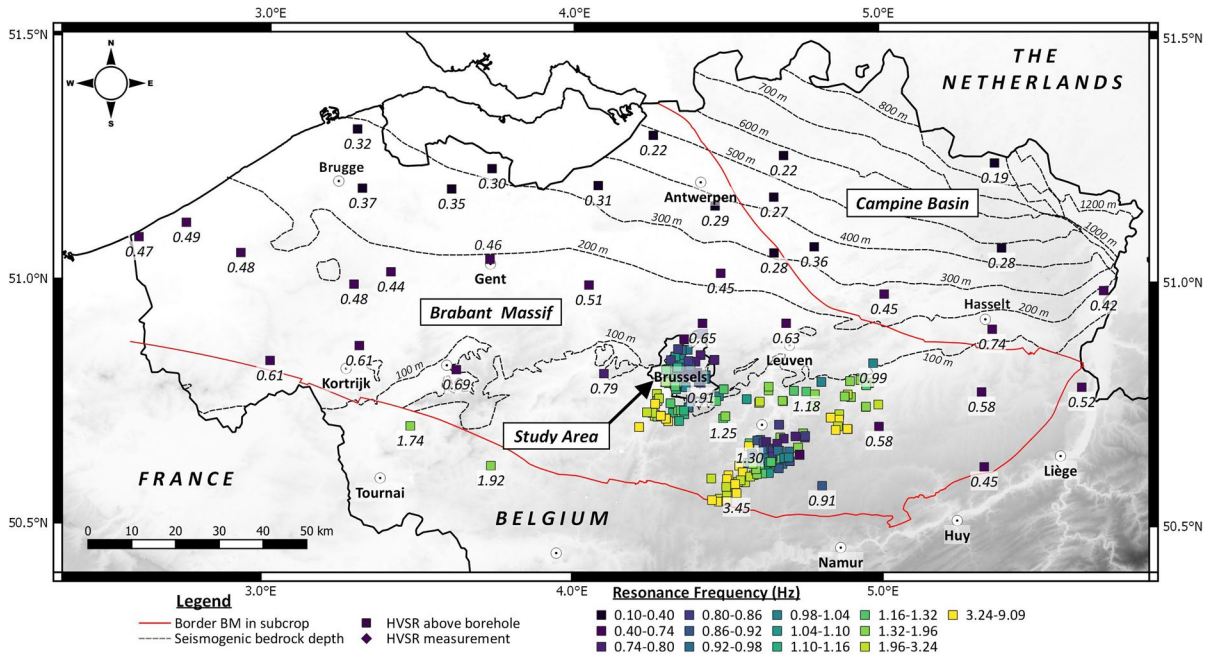

Fig. 1 Depth to the seismic bedrock (dashed grey lines). Seismic bedrock corresponds to the top of the Brabant Massif (BM) in Brussels and top of the Cretaceous in northern Flanders and in the Campine basin. Map composed from the G3Dv3 subsurface model of Flanders (Databank Ondergrond Vlaanderen 2020a). Resonance frequency (f_0) of 109 sites (diamonds) and 217 boreholes (squares) are shown (data from Nguyen et al. 2004, Molron 2015 and Van Noten et al. 2015b). The seismic bedrock dips to north and correlates with the decreasing f_0. The Brussels Capital Region forms the area of interest of this study

2.2 Soft-sediment cover stratigraphy

In the central and northern part of the Brussels study area, the erosional surface of the Brabant Massif is covered by white to grey Cretaceous chalk deposits. Most of the Cretaceous was eroded during the Middle Palaeocene uplift of the BM (Deckers & Matthijs 2016). South of the green dashed line in Fig. 2, the Cretaceous is mostly absent (sometimes Cretaceous remains in the deepest paleovalleys of the BM) and Cenozoic soft sediment layers directly cover the BM.

The Hannut Formation (HAN, upper Palaeocene) is the first formation to find above the BM. HAN's base consists of a gravel layer directly covering the BM bedrock. In the entire capital region, the clayey silt sediments of the Kortrijk Formation (KOR, early Eocene) can be found above HAN. The Brussels Sand Fm (BXL, middle Eocene) covers KOR in the eastern part of Brussels. BXL forms one of the main aquifers in Belgium for drinking water production (Peeters et al. 2010). The geomorphology of Brussels is strongly different east and west of the Senne river (Fig. 2). Whereas a hilly topography is present east of the Senne river, with hilltops up to + 139 m, the western area is 40 to 50 m lower. The reason for this geomorphological difference is the presence or absence of BXL, respectively, as it was partly eroded by the Senne river and was never deposited west of it.

In the eastern part of the Brussels Capital Region, the sandy to clayey of Sint-Huibrechts-Hern Fm (SHH, late Eocene–early Oligocene), the clayey-sandy Maldegem Fm (MAL, late Eocene) and the sandy Lede Fm (LED, middle Eocene) cover BXL. Some isolated hilltops in the NE of the area (Fig. 2) consist of SHH, LED and MAL directly on top of KOR without BXL in between.

Finally, fluviatile sediments (composed of sands and silts with clay/peat horizons) were deposited during the latest Quaternary glacial periods in the Senne valley and its tributaries (Fig. 2). These deposits can be up to 30 m thick in the Senne Valley. A thin Quaternary loess deposit with a mean thickness of 3–4 m thick covers the entire area outside the river valleys.

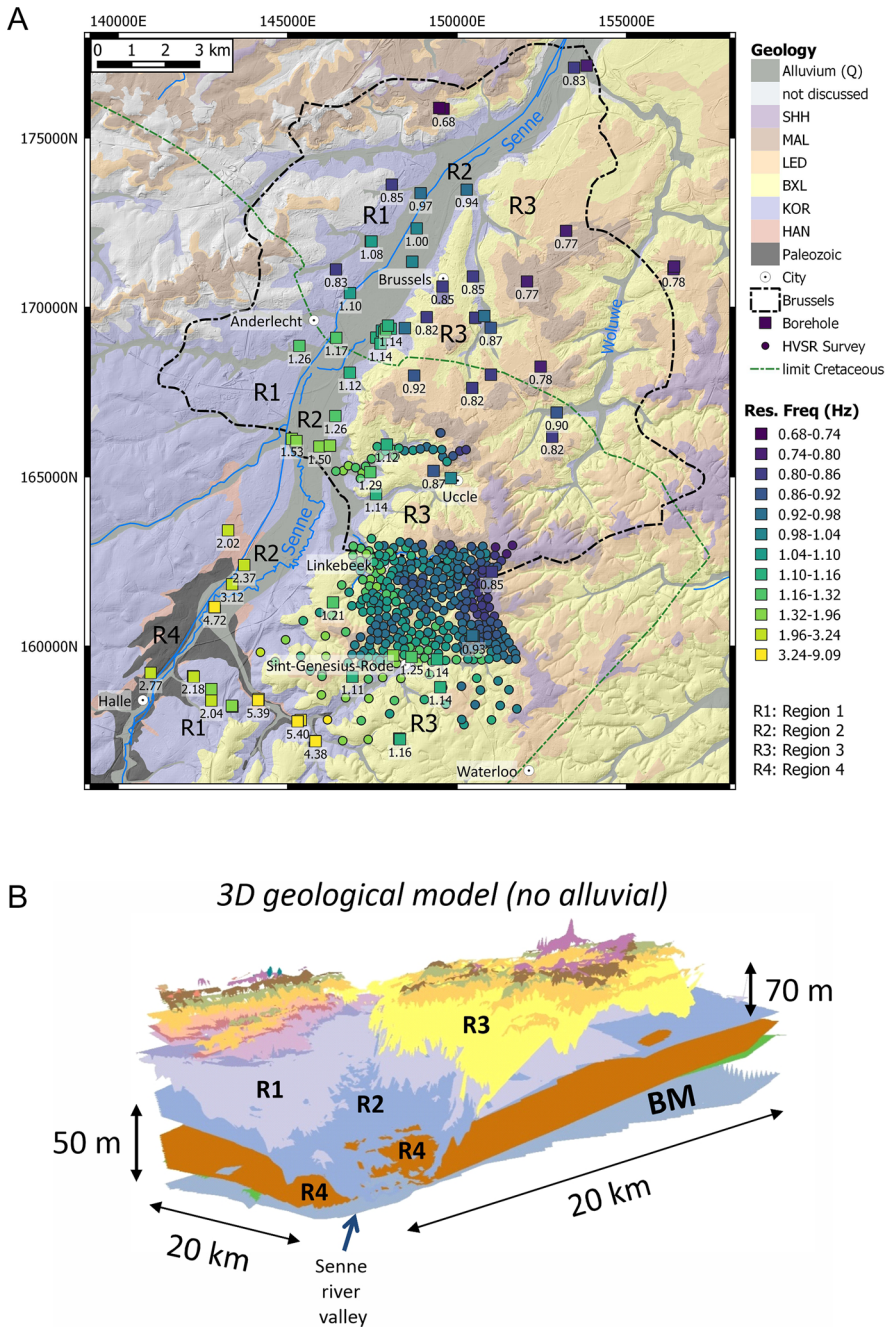

Fig. 2 (**Top**) Geological map of the study area. Squares indicate boreholes that reach the top of the Brabant Massif. Dots show the location of the HVSR bedrock depth mapping survey performed in this study. Symbols are coloured to the resonance frequency deduced from HVSR analysis of ambient vibration measurements. Stratigraphy from the Brustrati3D model (Devleeschouwer et al. 2017). R1 to R4 refer to the different regions discussed in this work. (**Bottom**) 3D geological model (not to scale, Cambier & Devleeschouwer 2013) that shows the soft sediment layering in the Brussels region. Stratigraphic colours correspond to the legend in the map above. Grey bottom layer represents the interpolated top of the Brabant Massif (BM) prior to this work

3 Data acquisition and analysis

3.1 Data acquisition

Temporal recordings of ambient vibrations were acquired. We used a single-station setup with a portable 24-bit digital (LEAS) Cityshark II acquisition system (Chatelain et al. 2000) mounted to a 3C LE-3D/5 s Lennartz seismometer. Sampling rate was set to 100 Hz. The Lennartz seismometers have eigen frequencies that are below the frequency of interest in this study, which justifies using this equipment. Duration of the ambient vibration recordings was 20 and 30 min for single point measurements and measurements above

boreholes, respectively. The gain level was adapted to the local conditions (noisy urban traffic versus calm rural environment) to avoid clipping. Position of the measurements were recorded by a Garmin™ handheld GPS or Smartphone location and afterwards controlled in Google Earth™. During windy days, the seismometer was protected against the wind using a circular plastic cap. In farmer's fields, a pile of grass was removed and the seismometer was placed on a 4-cm-thick, buried concrete plate to assure proper ground coupling.

Data of different HVSR campaigns are used. In Brussels, a detailed microzonation study was performed (Rosset et al. 2005; Petermans et al. 2006) in which ambient noise measurements were acquired above 74 sites located close to boreholes. 65 of these sites are integrated in this study. Nine sites were rejected because of inaccurate bedrock depth descriptions which could not be used for power law computation. The HVSR curves of these 65 measurements were recomputed to avoid methodological influences on the picked resonance frequencies and to ensure a consistent methodological approach. We extended this database with 23 new ambient noise measurements above boreholes acquired in 2017. Borehole bedrock depth information is retrieved from the databases of the Geological Survey of Belgium (2018), the Databank Ondergrond Vlaanderen (2020a) and BruStrati3D (Devleeschouwer et al. 2017). Electronic Supplement S1 summarises the information on boreholes that reach the basement and above which ambient vibration measurements were performed.

From August to October 2017, a geophysical survey was conducted during which 404 measurements of 20 to 30 min of ambient noise were gathered to create a bedrock paleorelief map. Measurements were performed near the small towns of Linkebeek and Sint-Genesius-Rode (Fig. 2). To grid the research area, a consistent station spacing of 200 m was used in a 15-km^2 area. To have some boreholes as an independent control in the survey area, the survey was extended to the South and Southwest by applying a 500-m station spacing coverage, which enlarged the entire survey area up to 25 km^2. In total, 66 days of fieldwork were performed.

3.2 Data analysis

Resonance frequency of each measurement was manually determined in Geopsy (Wathelet et al., 2020). The *H/V module* of Geopsy calculates the Fourier spectra of the horizontal, with H as the root mean square values of E-W and N-S components, divided over the vertical (V) component of ambient vibration. High-energy transient windows, e.g. cars passing, and electrical equipment running, are automatically rejected using the short-term average (STA)/long-term average (LTA) antitriggering tool (2 s STA, 30 s LTA). Window lengths (I_w) of 60 s were used. Data analysis occurred by selecting 50% overlapping windows. The H/V spectrum was manually improved by removing stronger transients that were overlooked by antitriggering (Chatelain et al. 2008). When not enough windows were available due to transient noise, I_w was lowered up to 30 s to increase the amount of windows (n_w). The 30-s window length was sufficient to have a stable curve in the lowest frequency range of the study area, i.e. 0.6–0.7 Hz. However, future users should be careful to shorten the window length when moving north of Brussels as too short noise windows can influence the stability of the HVSR curve in the low-frequency range (e.g., Mascandola et al. 2018). A 40% Konno and Omachi (1998) filter was used to smooth the spectrum of each H/V curve. Before interpreting the generated H/V curves, the SESAME (2005) recommendation guidelines were checked to be valid and if n_w was high enough for detecting a reliable H/V peak.

To increase the f_0 picking accuracy, we resampled the Geopsy output curve (.hv file) by performing a linear interpolation of the f_0-amplitude curve up to 15,000 samples using Python (see data availability for codes; Fig. 3). This interpolation results in a more accurate amplitude maximum (A_0) and f_0 than the default exported values in Geopsy. The standard deviation was maintained from Geopsy and represents one standard deviation generated by the variability of the selected individual windows. f_0, the error on f_0, A_0 and n_w were automatically exported from the .hv files into a database file (see Table S2 in the Electronic Supplement). This automation avoids manual mistakes while compiling the data from Geopsy and provides an easy output to be used in GIS. Afterwards, each point on the frequency-amplitude curve is converted to depth using the empirical frequency-depth power law relationship (see Sect. 4). This generates a virtual borehole (Fig. 3) in which A_0 is used as uncertainty on the impedance contrast between sediment and bedrock. We acquired the correct altitude of each measurement from the 1-m high-resolution

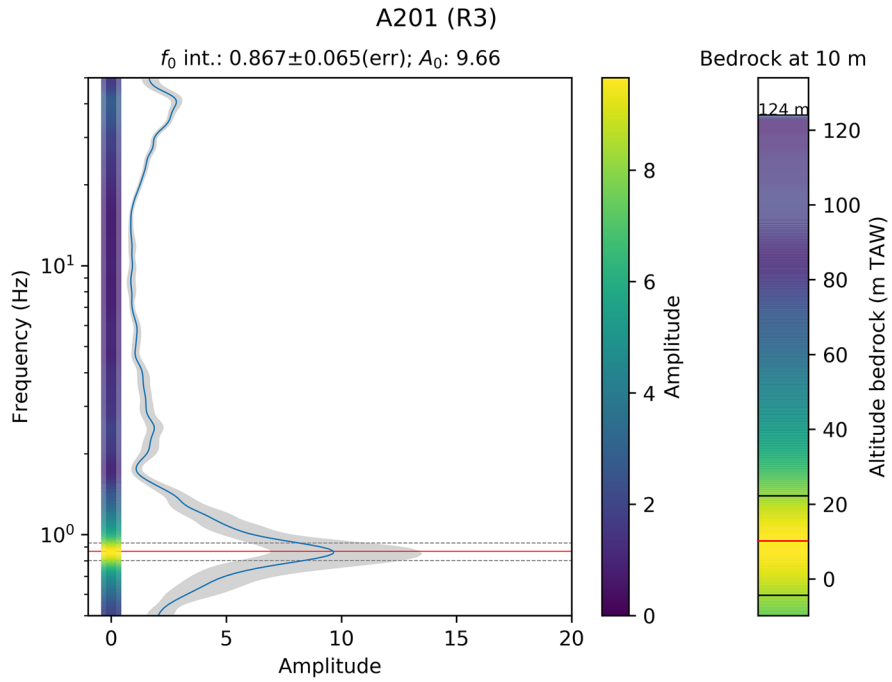

Fig. 3 Frequency–amplitude curve (blue curve). Standard deviation is represented by the grey-shaded area. The red horizontal line indicates maximum amplitude A_0 and interpolated f_0 (f_0 *int*) and is computed after resampling the .hv curve generated by Geopsy. The standard deviation on f_0 (err) is indicated by dashed grey lines. The frequency–amplitude curve is converted to a virtual borehole by using the frequency-depth power law relation R' developed in this study, with the amplitude as bedrock depth uncertainty. Example = Kleine hut borehole at Uccle, Brussels (A201; true bedrock at 0-m altitude, HVSR model predicts bedrock at 10 m altitude). TAW ('Tweede Algemene Waterpassing') = reference altitude in Belgium. See Electronic Supplement S3 for virtual boreholes of all data. See Van Noten et al. (2020) for the *HVSR to Virtual Borehole* python code to generate this figure

digital terrain model (Digital Elevation Model Flanders II, 2018; DTM) and then subtracted the obtained sediment thickness from that altitude to determine the absolute altitude of the bedrock. A virtual borehole of each measurement is available in the Electronic Supplement.

Apart from HVSR analysis, a complementary polarisation analysis was performed to deduce the azimuthal direction in which the H/V resonance peak has its maximum peak amplitude using the *H/V rotate* module in Geopsy. The directional H/V spectral ratio is calculated in 10° steps from north (0°) to south (180°). In the *H/V rotate* polarisation analysis, the same windows were used as in the *H/V module* avoiding to have transient sources in the signal trace that could influence this analysis. Each individual rotational H/V result was exported from Geopsy and replotted in an azimuth versus frequency polar plot (using Python, see data availability) to investigate site-specific directional resonance effects (Fig. 4). The maximum and minimum H/V amplitude at f_0 and their corresponding azimuths are automatically deduced from the data (see red and white dots in Fig. 4).

4 Defining empirical power law equations through regression

To obtain a reliable regression between resonance frequency and bedrock depth, we investigate two different possibilities: in the first option, only one regression line is derived through all f_0 that were gathered from measurements above boreholes in Brussels. In the second option, we separate the study area in four different regions based on the consistent geology within each region (see R1 to R4 in Fig. 2). For each dataset corresponding to these regions, a

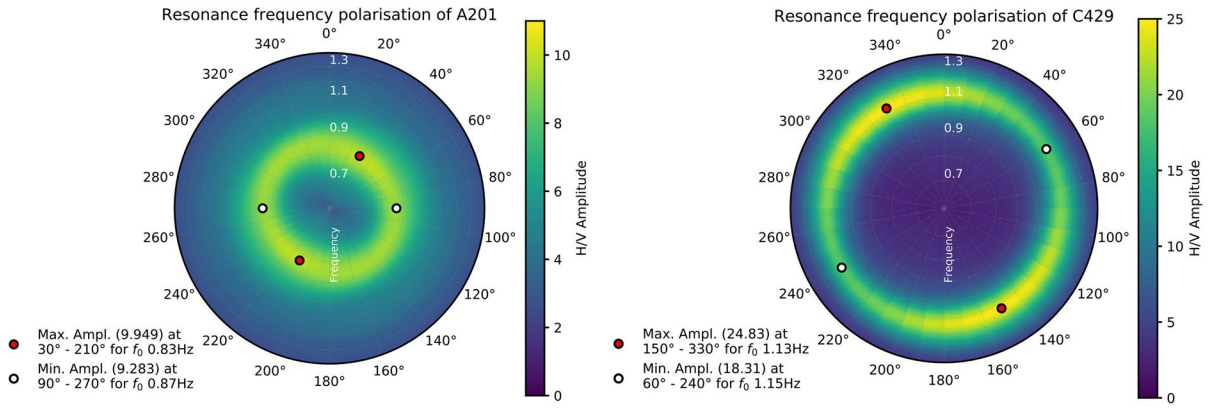

Fig. 4 Polarisation analysis of resonance frequency of two individual 20-min single station measurements. Red and white dots indicate azimuths in which respectively maximum and minimum peak amplitude occur at f_0. A201 (left) shows a uniform polarisation. C429 (right) shows a strong 150°–330° polarisation for f_0 and a significant higher impedance contrast at depth (higher A_0) compared to A201. See Electronic Supplement S3 for the polarisation plots of all data

separate regression is performed. The regions are as follows:

- Region 1 (R1): the area west of the Senne valley western area with KOR clays overlying HAN, and thus defining a dominant fine silt to medium silt to clayey lithology
- Region 2 (R2): the Senne valley and other smaller valleys area with a Quaternary lithology (mainly river infill) deposited on top of R1
- Region 3 (R3): the eastern area where upper Paleogene sandy formations (BXL, LED, SHH, MAL) cover the clayey/silty sediments of R1
- Region 4 (R4): only present in the southern part of the study area where either a recent lithology (Quaternary) of the Senne Valley or HAN directly covers the Palaeozoic basement rock of the BM

Because of heteroscedasticity of data, the f_0 versus bedrock depth data will show some departure from a perfect power law relation. It is important to note that bedrock depth (h) is the independent known variable from the boreholes and f_0 is the dependent variable, obtained through field measurements. To avoid attributing uncertainty of the dependent variable to the regression fit, an ordinary least-square linear regression of f_0 as a function of h is derived (Fig. 5). The error (one sigma) on f_0 is taken into account to weight the regression: i.e. smaller error results in a higher weight. We did not compute the reciprocal regression (h as function of f_0) as this would generate a different best-fit line because of the different uncertainty on h (Bauer et al. 1992). Hence, the best fit provides a spread of frequencies that gives a true error estimate of f_0 compared to h. Also R^2, i.e. the statistical factor that explains the quality of the fit, is computed.

Figure 5 and the equations below present the results of the different regressions through the data. The regressions are restricted to the range of thicknesses (vertical brackets in below) that is available for each region. For the four geology-dependent empirical equations between depth and f_0, the obtained power law relations are (with h in metres and f_0 in Hz):

$$(\mathbf{R}1)\ h_1 = 87.576 f_0^{-1.663} \quad \left(R^2 = 0.975\right) \ [7.0\text{m} - 117.3\text{m}] \tag{3}$$

$$(\mathbf{R}2)\ \mathrm{h}_2 = 88.486 f_0^{-1.735} \quad \left(R^2 = 0.851\right) \ [40.5\text{m} - 133.7\text{m}] \tag{4}$$

$$(\mathbf{R}3)\ h_3 = 90.422 f_0^{-1.641} \quad \left(R^2 = 0.901\right) \ [65.5\text{m} - 175.9\text{m}] \tag{5}$$

$$(\mathbf{R}4)\ h_4 = 200.00\ .\mathrm{f}_0^{-2.028} \quad \left(R^2 = 0.483\right) \ [3.0\text{m} - 21.0\text{m}] \tag{6}$$

We also computed one regional empirical equation R derived through all data points:

$$(\mathbf{R})\ h = 91.453.\mathrm{f}_0^{-1.633} \quad \left(R^2 = 0.914\right) \ [3.0\text{m} - 175.9\text{m}] \tag{7}$$

The data points of R4 (rose dots in Fig. 5) are much more strongly scattered than the data points of the other regions. R4 groups Quaternary deposits and the Hannut Fm above the Brabant Massif.

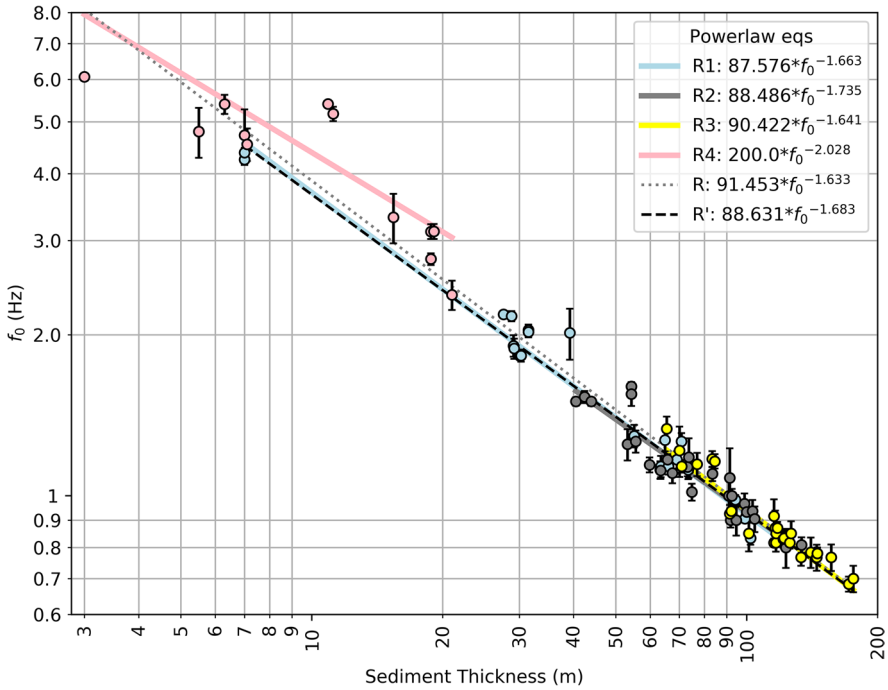

Fig. 5 Best fit regression through resonance frequency (f_0) in function of sediment thickness (h) known from boreholes. Six power law regression lines are deduced: full coloured lines represent regressions through boreholes from regions (R1, R2, R3 and R4. The grey dashed line R is the regression through all data points. The black dashed line R' is the regression through regions R1, R2 and R3. Total amount of boreholes used = 88. See online version for colour notations (same colours applicable for all figures)

R4 has a large lateral lithological variability with different geotechnical properties than the other three groups. Because of this scattering, regression R4 has more difficulty to reproduce the data points. Including R4 data in the regional regression R (grey dashed line in Fig. 5) tends to overestimate the thicknesses of the other regions. The R^2 value of R4 suggests a poor thickness prediction and hence defining a unique power law in this region may not be feasible, even if more data points would be acquired. Hence, to avoid the influence of R4 on the regression, we also computed a regional regression R' (black dashed line in Fig. 5) without including the data of R4, which results in the following PR:

$$(\mathbf{R}')\ h = 88.631 f_0^{-1.683}\ \left(R^2 = 0.975\right)\ [7.0\text{m} - 175.9\text{m}] \quad (8)$$

R' has the largest R^2 value of all regressions, suggesting a very good prediction quality.

To evaluate the prediction quality of these power law relations, the residual between the true bedrock depth (h_{True} known from the boreholes) and predicted bedrock (h obtained by the power laws) is computed, both for the regional power law equation (white dots in Fig. 6A; h_{1eq} in Fig. 6B) and for the different geology-dependent power laws (coloured symbols in Fig. 6A; $h_{geol.eqs}$ in Fig. 6B). These residuals show the real scatter (expressed in percentages) of the prediction and evaluate how much the different power law relations under- and overestimate the true sediment thickness. Such an evaluation is useful for users that want to use these power law relations to predict bedrock depth. The biggest error on the depth estimation largely depends on the used dataset and can be related to the lateral variability in Vs of the geological system which causes an imperfect fit through the data.

For the Brussels dataset, the maximum offset from the true sediment thickness ranges between 27% thickness underestimation and 19% thickness overestimation for R1, R2 and R3 and up to more than 50% for R4. On average, the PRs have an uncertainty of 9% in overestimating and 8% in underestimating the bedrock depth. One must keep in mind this error when using power law equations for bedrock depth modelling.

One may evaluate which power law would be best suited to predict bedrock depth in a region, by computing the difference between residuals of one power law ($h_{True} - h_{1eq}$) and the residuals of the geology-dependent power laws ($h_{True} - h_{geol.\ eqs.}$). This difference is illustrated in a histogram with 0.5-m binning in Fig. 6B. This illustration may

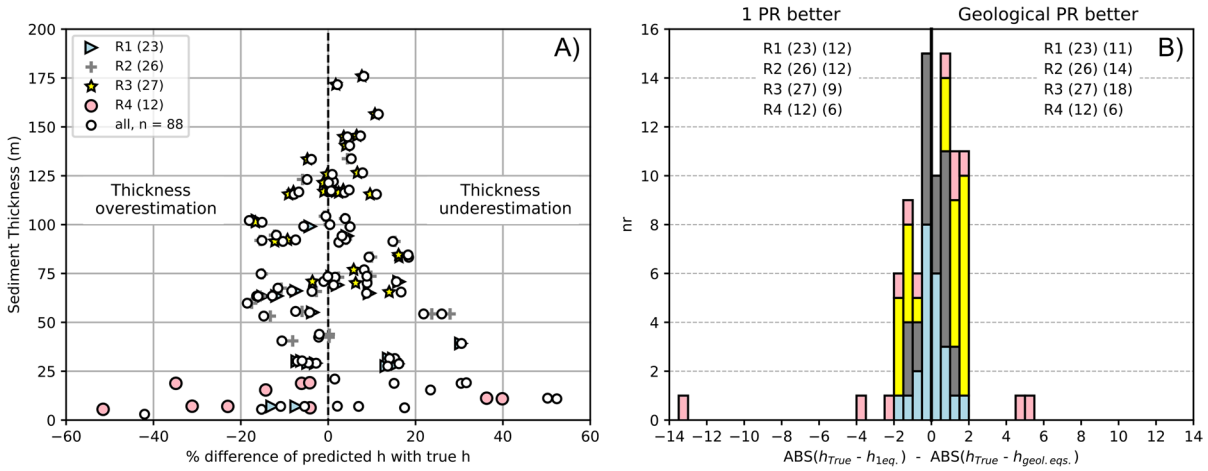

Fig. 6 **A** Comparison of true sediment thicknesses (h), obtained from borehole data, and predicted sediment thickness, computed using the power law relations derived in Fig. 5. Coloured symbols represent the data from individual power law relations; white dots are computed using power law relation R'. Negative percentages indicate thickness overestimation; positive percentages indicate thickness underestimation. **B** Residual histogram evaluating whether using one regional power law relation (R'; h_{1eq}) would predict bedrock depth better than using geology-dependent power law relations ($h_{geol.\ eqs.}$). Numbers in brackets indicate the amount of points on each side of the histogram. ABS = absolute values

be convenient because the power law relation that best predicts the true thickness will show the highest distribution. For the Brussels case, for 56% (49 data points), the geology-dependent PRs (R1, R2, R3, R4) predict slightly better bedrock depth than the regional PR (R'; 44% of the data; 39 points). However, because R4 should not be used and R' has a very high R^2 value, we cannot make any strong arguments to favour the geology-dependent PRs above R' to convert resonance frequency to depth.

Using Eq. 1, the average *Vs* as a function of *h* of the used boreholes is computed to demonstrate the (inter)dependency of the different datasets of the regions (Fig. 7). The four geology-dependent power law relations and error bars are converted as well.

5 Bedrock paleorelief: case study south of Brussels (Belgium)

5.1 Resonance frequency to depth

To verify if the constructed power law relations can be applied in the case study area where the 404 ambient noise measurements were gathered, the HVSR data distribution of the survey and the boreholes are compared in histograms. The range of frequencies (0.65 to 5 Hz) that was used to compute the power law relations (Fig. 8 bottom) fully covers the range of frequencies that were studied in the case study (Fig. 8 top). One should be careful in using power law relations that were created in another frequency range than where a microzonation survey is held as the

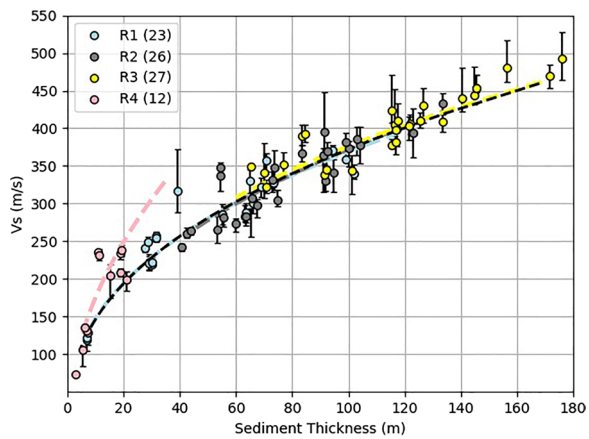

Fig. 7 Estimated variation in average shear wave velocities (*Vs*) and their error range (error bars) with increasing sediment thickness deduced from ambient noise measurements above boreholes in the Brussels Capital Region (Belgium). Coloured dashed lines are geology-dependant power law relations (R1, R2, R3, R4) converted to *Vs*. Dashed black line is the regional power law relation R' converted to *Vs*

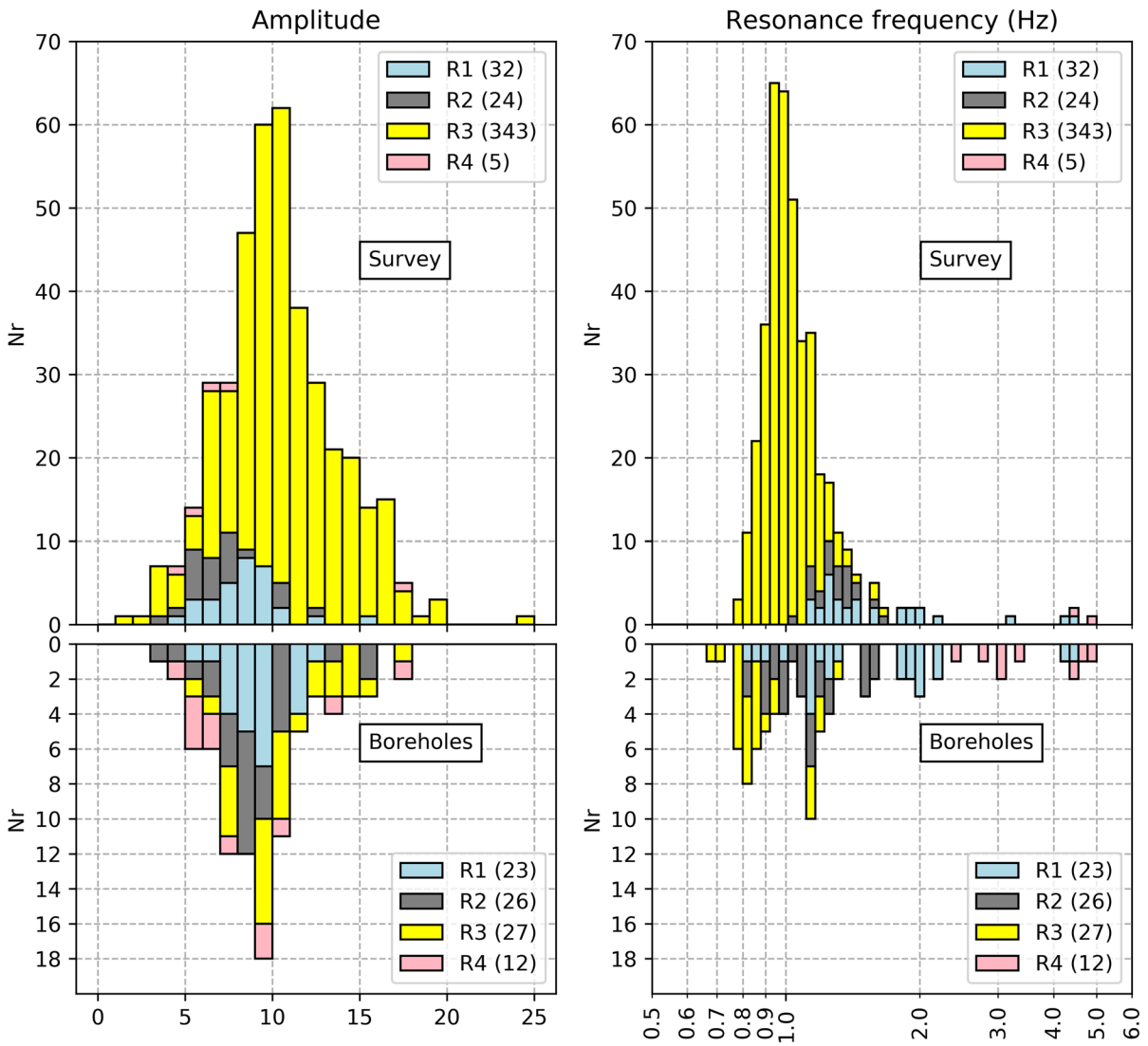

Fig. 8 HVSR amplitude (left) and resonance frequency (right) histograms obtained from ambient noise measurements in the survey area (top) and above boreholes (bottom). Colours represent the four different considered regions (R1 to R4). The histogram data representation allows evaluating if a different power law relation of a region is supported by enough borehole data measurements to predict bedrock depth in the survey area

regression may not be qualified to predict the bedrock depth. Most data was gathered in R3. Because the regional power law R' (Eq. 8) has a higher R^2 value than the geology-dependent power laws R1, R2 and R3, we decided to take R' to convert resonance frequency to depth for the case study.

The HVSR survey data demonstrates the strong impedance contrast between the sedimentary cover and the bedrock of the BM. For most data, A_0 is very well expressed and shows a normal distribution with a mean H/V peak amplitude of 10 (Fig. 8, left). There is no spatial, nor a geological correlation between f_0 and A_0. HVSR analysis results in a wide range of resonance frequencies (between 0.79 and 5.40 Hz; Fig. 8, right). The f_0 peaks are mostly strong and narrow. The strong impedance contrast makes HVSR an ideal tool in identifying the BM bedrock in Central Belgium where overlain by a sedimentary cover.

The location of the HVSR campaign with respect to the local geology is shown in Fig. 9A. First, a resonance frequency map (Fig. 9B) was

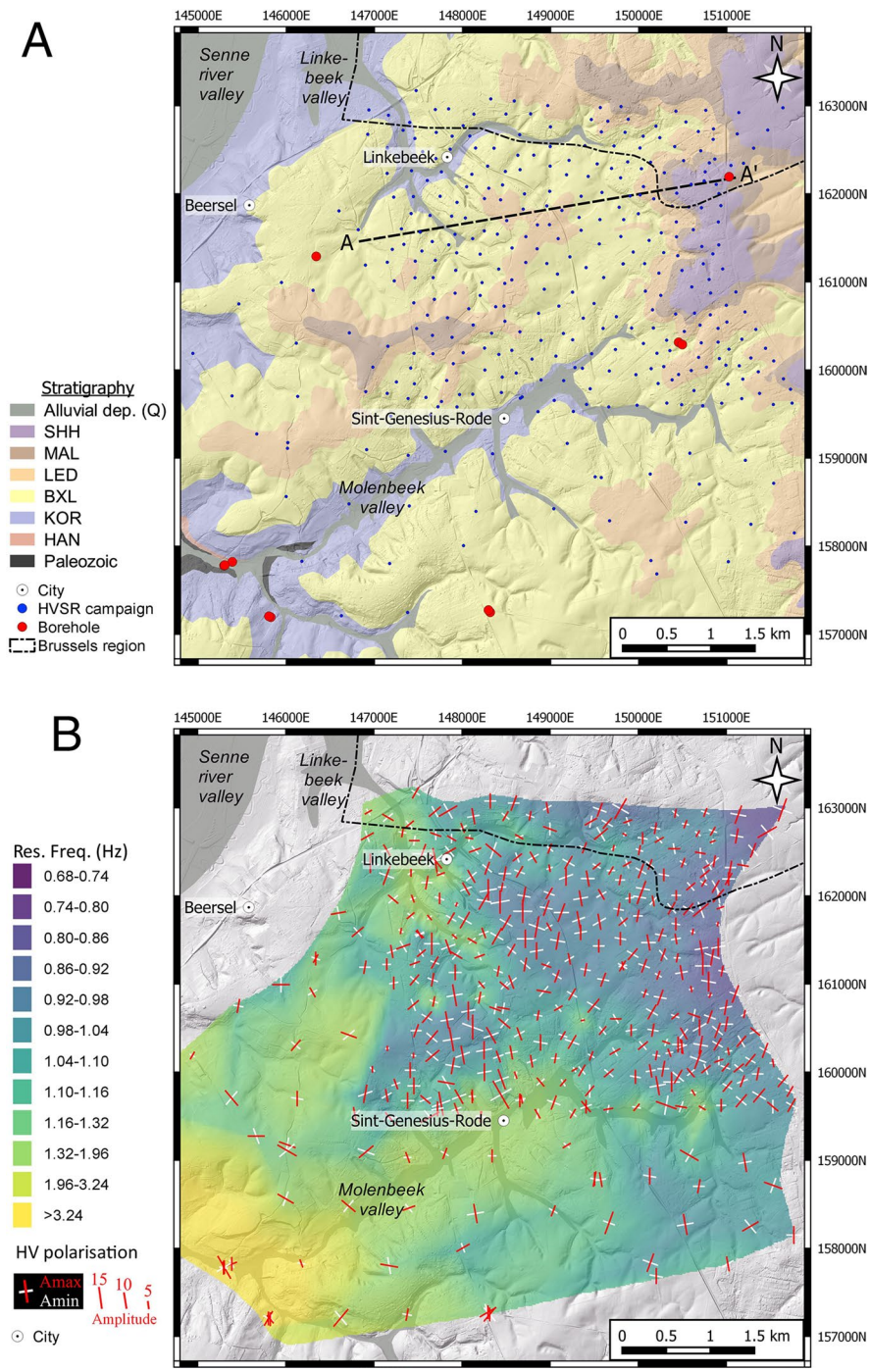

Fig. 9 **A** Overview of 404 survey locations (blue dots) shown on the local geological map (Brustrati3D model; Devleeschouwer et al. 2017) overlain on a hillshade map of the local DTM (Digital Elevation Model Flanders II, 2018). Red dots are borehole locations. See Fig. 2 for location. See Electronic Supplement for raw data. Profile A-A' shown on Fig. 12. B Interpolated resonance frequency map with hillshade map in the background. Polarisation of H/V amplitude is shown by red (maximum A_0; Amax) and white (minimum A_0; Amin) lines. Length of the polarisation lines scales to A_0. Background map shows the 1-m high-resolution Digital Terrain Model (Digital Elevation Model Flanders II, 2018). C Interpolated sediment thickness map obtained by converting resonance frequencies to sediment thickness using the regional power law relation R' (Eq. 8). Background map shows the 1-m high-resolution Digital Terrain Model (Digital Elevation Model Flanders II, 2018). D Brabant Massif bedrock paleorelief map (natural neighbour interpolation) in m TAW. Note a 1.5-km-long NNW-SSE trending ridge between Sint-Genesius-Rode and Linkebeek. Dashed line indicates the contact between Tubize (TUB) and Blanmont (BLM). Formations deduced from gravimetric and aeromagnetic observations (see Fig. 11). Cross-section A-A' shown in Fig. 12

created by applying a Natural Neighbour Interpolation (NNI; cell size 10 m) between each f_0. At the edges and outside the survey area, interpolated values are not expected to be valid due to interpolation effects and the map was cropped. The NE part of the survey area shows the lowest f_0 whereas the western part and the Molenbeek and Linkebeek incised river valleys show the highest f_0. Second, a sediment thickness map was created by converting all individual f_0 to depth using R' (Eq. 8) and

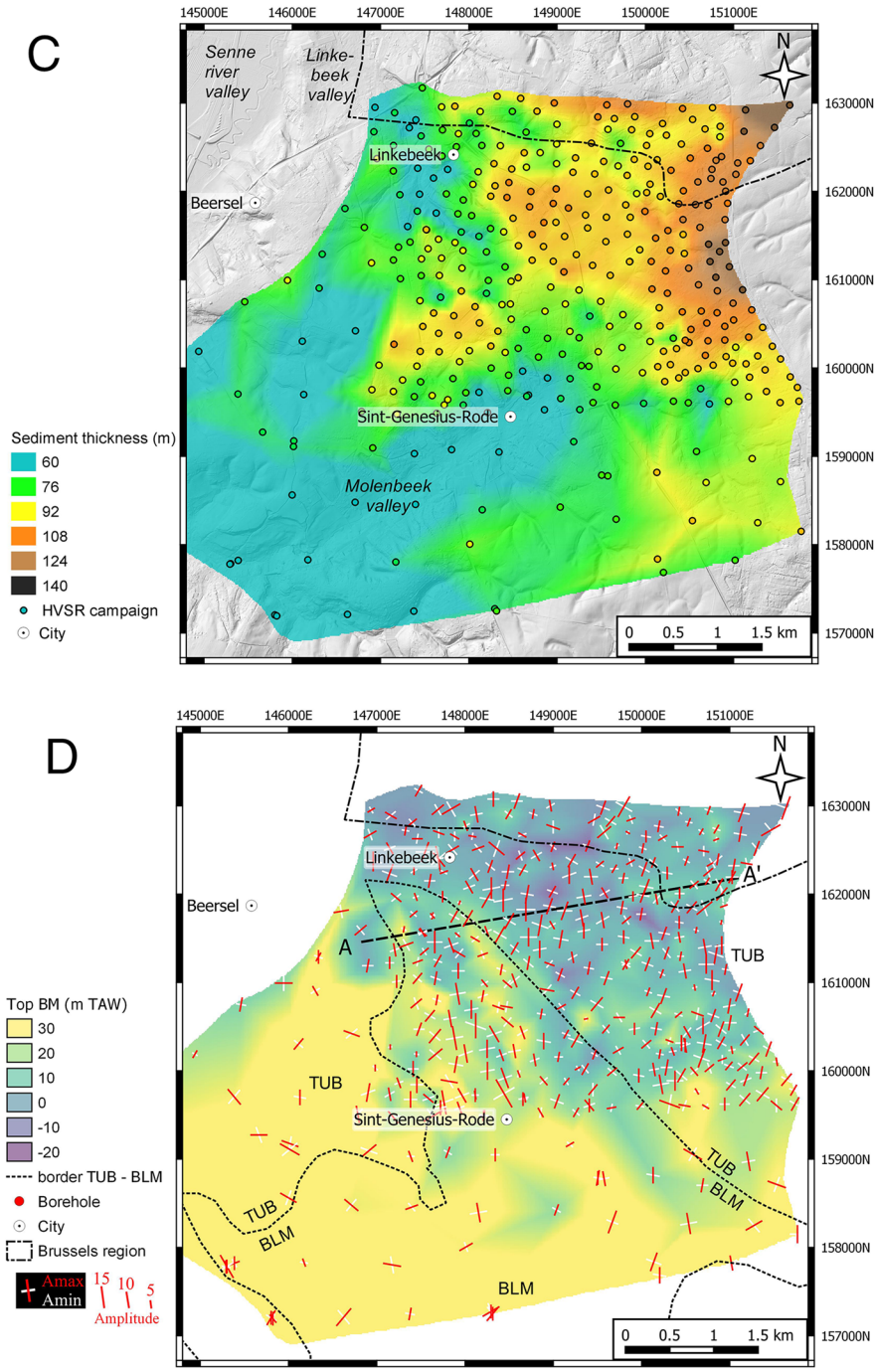

Fig. 9 (continued)

applying a NNI interpolation between the points. The resulting sediment thickness map (Fig. 9C) resembles the topographical map with the highest topography/thickest sediment cover in the NE and the lowest topography/thinnest sediment cover located in the W and in the incised river valleys. Because data points are too widely spaced (200 m), the detailed shape of the incised rivers is only poorly resolved.

Third, to create the bedrock paleorelief map (Fig. 9D), the obtained sediment thickness of each

point is subtracted from the altitude of each point derived from the local DTM map. Then, the bedrock paleorelief map was interpolated using NNI. We deliberately did not subtract the sediment thickness map in Fig. 9C from the DTM as the detailed high-resolution topography would imprint too strongly on the final bedrock paleorelief map.

The bedrock paleorelief map shows the following features: the top of the BM dips from ~ + 30 m in the South to ~ − 20 m in the North. Few isolated outliers are detected which even show a strong variability of the paleorelief in short distances (e.g. converting the f_0 of B120 to depth gives a hill of 10 m higher than the surrounding points; see Fig. S1 in the Electronic Supplement for location). In the southern area with the 500-m station spacing, the map seems to be less good resolved to make small lithological interpretations; nevertheless, all points consistently show the highest bedrock altitude from the entire survey. This is correlated with the boreholes in the studied area.

Within the 200-m station spacing area, several contrasts are detected. The most obvious observation is a 1-km-long NNW-SSE-oriented ridge situated between Linkebeek and Sint-Genesius-Rode. On average, the top of this ridge stands out 20 m above the surrounding bedrock (Fig. 9D). West of the ridge, a paleovalley is present parallel to the ridge. In the southern part of the survey area, bedrock altitude is higher (up to ~ + 30-m altitude).

5.2 Polarisation analysis

The azimuthal direction in which f_0 has its maximum peak amplitude is shown in Fig. 9B and D for each HVSR measurement. Both the orientation and size of the maximum (red lines on Fig. 9B, D) and minimum (white lines on Fig. 9B, D) H/V amplitude are evaluated. A weak polarisation is present with A_0 in the minimum energy direction at 75 to 90% relative to the maximum energy direction. Strongest polarisation occurs in A351 (see Fig. S1 in Electronic Supplement for location) where A_0 is twice as large in the maximum direction (Fig. 10B). Polarisation is on average oriented between N10°–N190° and N20°–N200°. This polarisation is linked to the direction that has a maximal energy contribution to the ambient seismic noise. Although small deviations could likely be linked to imperfect seismometer placement during field work, the polarisation is obvious: in areas with a rather flat bedrock paleorelief, the polarisation orientation is well defined and constant.

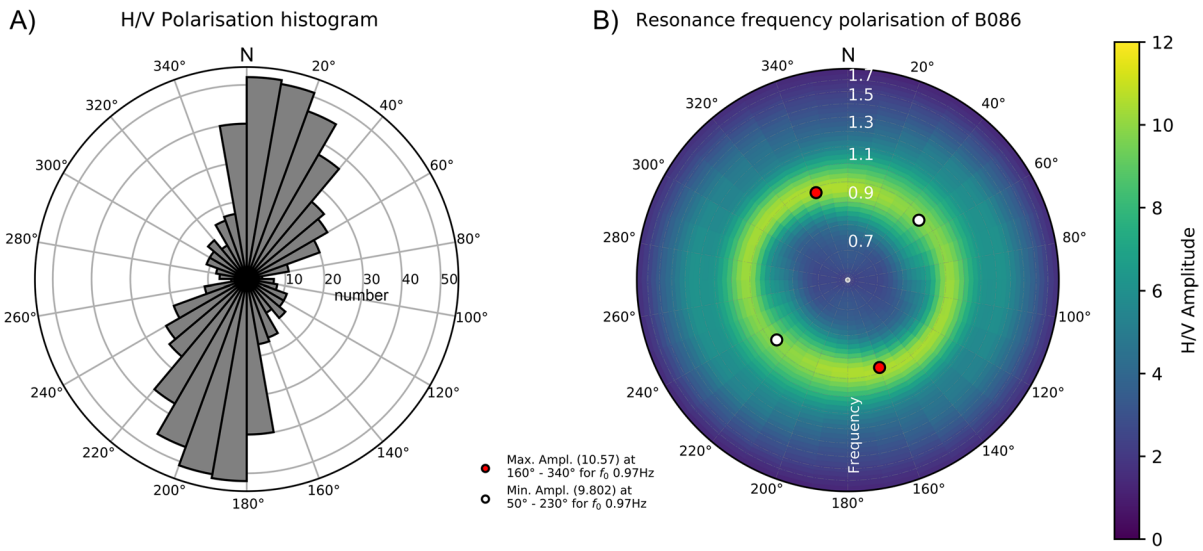

Fig. 10 **A** H/V polarisation histogram showing the distribution of azimuthal directions in which the resonance frequency has its maximum peak amplitude. The maximum energy is dominantly oriented N10–20°, pointing towards the main urban source of Brussels. See Electronic Supplement S3 for all individual measurements. **B** Example of a HVSR measurement (B086) on top of the ridge with an azimuthal direction diverging from the regional trend. Python code to plot this polarisation diagram is available on Github (see data availability)

Around the NNW-SSE-oriented ridge, however, the polarisation is weaker and maximum polarisation orientation deviates from its regional trend and is scattered. H/V amplitudes are smaller on the ridge and larger in the paleovalley SW of the ridge. This change in polarisation indicates that the protruding bedrock here deflects the local radiation of seismic energy. Also in the Linkebeek and Molenbeek river valleys, amplitudes are smaller and a clearly defined polarisation orientation is absent. This is likely related to a local deviation induced by the alluvial deposits in these incised river valleys.

6 Discussion

6.1 Using potential field data to explain the paleorelief

In our derived bedrock paleorelief model (Fig. 9D), a 1-km-long, NNW-SSE-oriented (~N20°W), 20-m-high bedrock ridge is detected at ~100-m depth. To understand to which host rock this ridge corresponds and how its orientation can be explained, we compare the Brabant Massif paleorelief shown in Fig. 9D with Bouguer anomaly and aeromagnetic data (Fig. 11). The Bouguer map (Fig. 11, left) is a residual map composed by subtraction of the anomaly field, upward continued to a height of 1 km above the ground, from the Bouguer anomaly. This filter technique highlights shorter wavelengths, and hence superficial structures, and hides deeper, regional structures (Van Noten et al. 2015a). The Tubize (TUB) and Blanmont (BLM) formations (see Sect. 2.1) can be identified as follows:

- The quartzitic units in TUB have a low density (negative gravity values) and a strong positive aeromagnetic value due to the presence of magnetite in the quartzites. More slaty parts have a higher

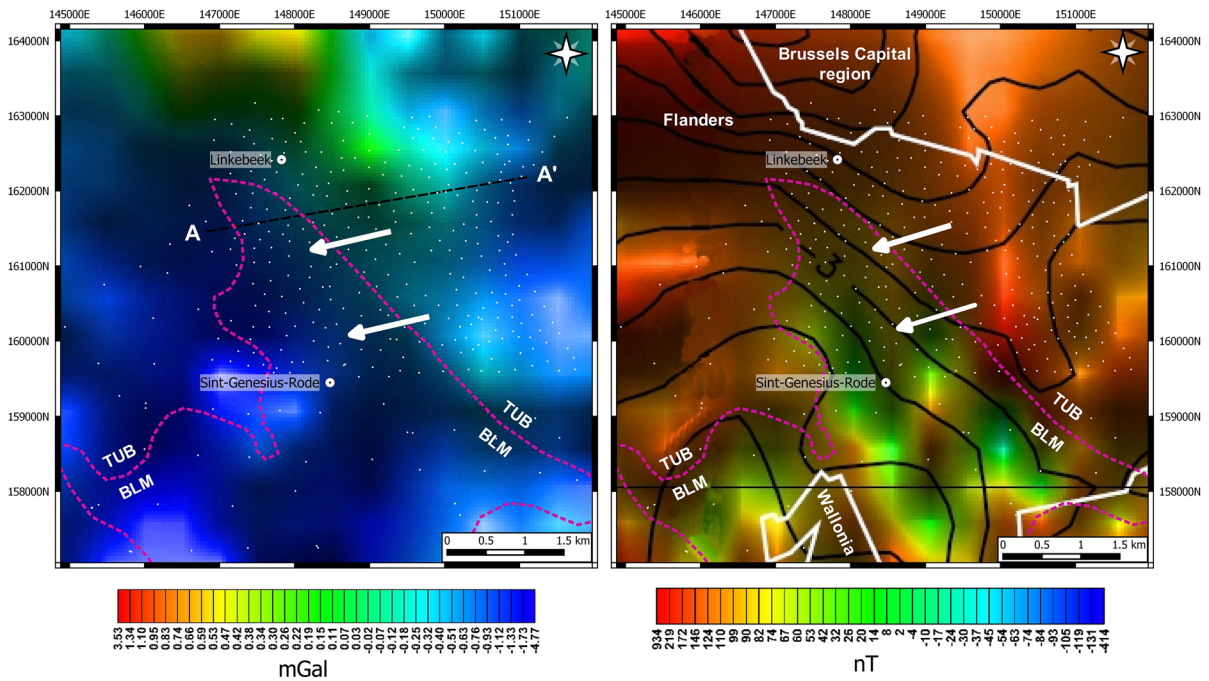

Fig. 11 Potential field data of the HVSR study area. White dots: HVSR survey points. (**Left**) Residual Bouguer gravity map, short-wavelength filtered (subtraction of 1 km upward continuation from Bouguer anomaly) (Chacksfield et al. 2004; Databank Ondergrond Vlaanderen, 2020b; Williamson et al. 2004). (**Right**) Aeromagnetic map (reduced to the pole; Chacksfield et al. 1993; Everaerts 2000). Black lines show contour lines. Combining both maps allows defining local stratigraphy of the Brabant Massif and interpreting the paleorelief of the Brabant Massif. TUB: Tubize Formation; BLM: Blanmont Formation. Purple dashed line: interpreted border of TUB and BLM. White arrows indicate the location of the NNW-SSE trending ridge observed in Fig. 9D. Scale similar to Fig. 9

(sometimes positive) gravity value and remain their magnetic signature.
- The quartzites of BLM are expressed with negative aeromagnetic and strong negative gravity values.

These gravity values are valid as a rule of thumb; however, one has to be careful to compare Bouguer values as the overall Bouguer gravity signature is cumulative and can be influenced by rock that is buried deeper: e.g. in regions where BLM is shallowly buried below TUB (e.g. close to their contact), TUB will be more negative. Changes between units are not always sharp but can be gradual related to transition from one formation to another (e.g. the upper part of BLM is magnetic highlighting a gradual transition from BLM to TUB).

Right in the middle of the 2017 survey, the encountered NNW-SSE-oriented ridge corresponds to low Bouguer gravity values and negative aeromagnetic values, i.e. values representative for the hard and steeply-dipping quartzites of BLM. East of the NNW-SSE ridge, sharp boundaries between Bouguer gravity values and between aeromagnetic values exist, indicative of a steep bedding contact between BLM and TUB (purple dashed line on Fig. 11). The area NE of the ridge overlaps with a positive aeromagnetic anomaly and can be linked to a less-resistant, slaty part of TUB. This area is lower on the paleorelief map because of being less resistant to erosion compared to BLM. The southern part of 2017 survey is higher on the paleorelief map and this area reflects the hard quartzitic part of TUB.

Based on this comparison between the paleorelief and the aeromagnetic and Bouguer gravity data, the following local stratigraphic implications can be made:

- The lower part of BLM has a low density, is very hard and non-magnetic.
- The upper part of BLM has a low density, is very hard but appears to be magnetic.
- The lower part of TUB has a low density, can be hard and is strongly magnetic.

To visualise our observations, a cross-profile A-A' was made: Fig. 12A shows virtual boreholes, converted from HVSR measurements using PR R' (Eq. 8), and laterally projected on profile A-A'. The surface of these virtual borehole sometimes not perfectly coincides with surface of the profile. Figure 12B presents an interpretation including the surface variation, soft-sediment stratigraphy

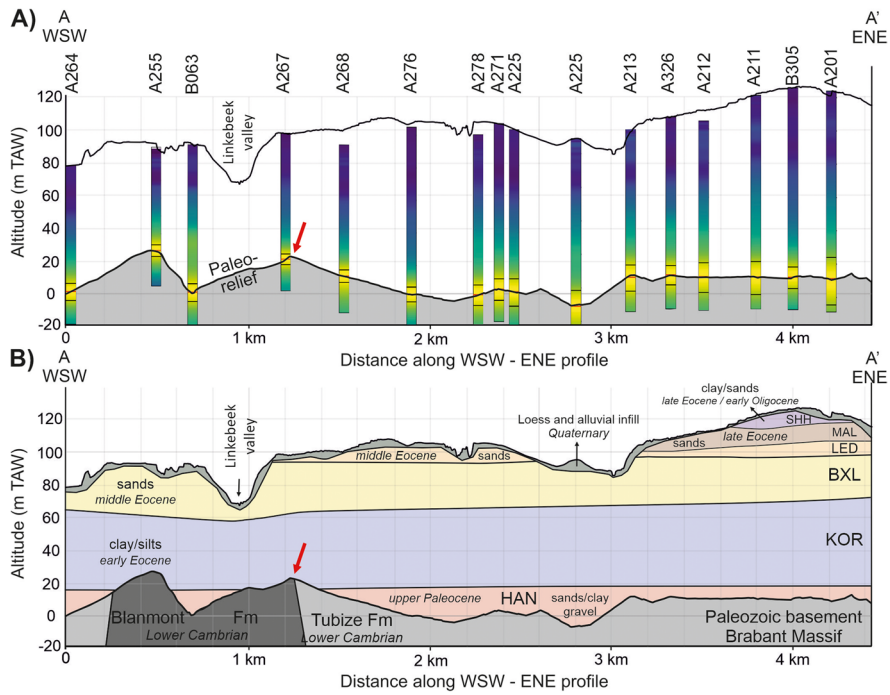

Fig. 12 **A** Virtual boreholes (20 min H/V amplitude bars converted to depth using power law equation R') projected laterally on cross-section A-A' (see Fig. 9A). On each virtual borehole, bedrock depth uncertainty is indicated by the black horizontal lines. Paleorelief derived from Fig. 9D. **B** Interpretation of the paleorelief using potential field data shown in Fig. 11. Soft-sediment stratigraphy obtained from the Brustrati3D model (Devleeschouwer et al. 2017). The red arrow shows the position and interpretation of the ridge standing out of the paleorelief. Vertical exaggeration: 5×

and interpolated paleorelief of the Brabant Massif. The structure of the bedrock is interpreted from the potential field data analysis.

Throughout the core of the Brabant Massif, several other NNW-SSE trending ridges occur, either in outcrop in incised river valleys (Piessens et al. 2004), or in the subsurface and detected by potential field data (Matthijs et al. 2005). These ridges relate (i) to the upright orientation of folds (Sintubin et al. 1998; Debacker et al. 2004; Debacker 2012) and differential erosion of TUB and BLM, and (ii) to local shear zones. Ridges (i) have been drilled by two boreholes (boreholes 88W750 and 88W1057 in Buffel & Matthijs, 2009), in which a higher relative abundance of quartzites was detected, and (ii) were detected by observing higher f_0 values along a HVSR profile in the Senne Valley (Rosset et al. 2005; Petermans et al. 2006). Hence, our paleorelief fits well to the general structure of the Brabant Massif.

6.2 Influence of subsurface structures on ambient noise

The ridge is not only evidenced by f_0 to depth conversion but also by the azimuthal dependency of f_0. Underground structures (ancient paleovalleys, faults or a heterogeneous geology) and surface rock ridges can guide or diffract seismic waves and create an azimuthal dependency of seismic noise. Close to faults and surface ridges, A_0 is maximal perpendicular to the structure and strong ground-motion amplifications are deduced (Pedersen et al., 1994, Massa et al. 2010, Matsushima et al. 2014, Paratore et al. 2013). In paleovalleys, A_0 is maximal parallel to the length axis of the valley (Hollender et al. 2015; Cauchie et al. 2017). In our study area, the general N10-20° azimuthal preference in the investigated frequency band can be linked to the seismic source (urban area of Brussels Capital). However, close to the NNW-SSE-oriented ridge, polarisation is much weaker (Fig. 9D) and the maximum amplitude strongly deflects. We conclude that the ridge acts as a wave guide (similar to surface ridges) and scatters the propagation of seismic waves. After all, there would be no reason that seismic waves would propagate around or above the ridge without interacting with it. Due to the high impedance contrast between the sediment and the BM, this wave deflection is strongly represented in the azimuthal dependency of f_0. Hence, in microzonation studies where one has a change in the polarisation of the HVSR amplitude, the method clearly can indicate the presence of anomalous features at depth.

6.3 Using geology-dependent or regional power law relations?

In the Brussels survey area, the different power law relations (Eqs. 3–5) of regions R1, R2 and R3 only slightly differ. In R3, i.e. the region where BXL, LED, SHH and MAL formations occur, sandy formations cover the R1 sands/silts/clays of KOR and HAN. In R2, alluvial sediments cover the KOR clayey formations of R1. Hence, the reason why the different generated power law relations are rather similar is related to the fact that the geology in the three defined regions is not independent from each other because R1 underlays the entire studied region. In our case study, we eventually did not apply the geology-dependent power law relations because the HVSR survey overlapped different regions and R' performed slightly better.

To decide if either a regional or a local geology-dependent power law relation should be used in a microzonation study, it is thus advised (i) to compute R^2 values of the regression; (ii) to compare the residuals between the true bedrock depth obtained from boreholes and the predicted bedrock depth; and (iii) to investigate if the HVSR measurements from which the power law is constructed is representative for the area in which the microzonation survey is performed.

7 Conclusions

We evaluated the power law relation between sediment thickness and borehole-controlled polarised resonance frequencies (f_0). We also investigated if power law relations developed for different soft-sediment geological regions would improve the accuracy of predicting the bedrock depth instead of developing one regional power law relation. The methodological investigations resulted in the following conclusions:

- To construct a reliable power law relation, it is advised to incorporate the error on f_0 to weight the regression and, afterwards, to evaluate calibration errors to quantify the under- or overestimation of the regional and individual bedrock depth predictions.
- Before applying a power law to a survey area, it is advised to evaluate if enough boreholes can be used in that area to support the developed power law regression.
- If one lacks sufficient borehole data to create geology-dependant power laws, it is still better to develop a regional power law relation instead of using a regression from another study area.
- Microzonation surveys strongly benefit from a polarisation analysis of the azimuthal dependency of the resonance frequency. When anomalous features are present in a paleorelief, the seismic wavefield is polarised around the anomaly and the polarisation analysis allows highlighting these anomalies.

An ambient noise survey south of Brussels (Belgium) was performed to map out the paleorelief of the Brabant Massif at depth. Applying the methodology leads to the following conclusions:

- Separating the HVSR data into different regions and constructing geology-dependent power law relations did not improve the accuracy in predicting the bedrock depth in Brussels. This is because the geology of one region (R1; dominated by the clayey Kortrijk Formation) occurs below the entire investigated region (except in R4). Hence, the different selected regions are geologically not entirely independent (i.e. compare the tabular geology to a layered cake) and share a common factor in the shear-wave velocity. For areas with an independent geological soft-sediment composition (and hence different *Vs* for each region), it is advised to at least investigate to separate the power law relations provided enough boreholes are available to support the regression.
- In Brussels, the regional relation $h = 88.631.{f_0}^{-1.683}$ (R') can be used to convert resonance frequency to depth, with an error of ~ 10%. For region R4 (Hannut Formation or alluvium above bedrock), the power law correlation factor is too low and variability of the lithology prevents composing a reliable power law relation.
- South of Brussels, a 200-m spacing single station campaign in a 25-km^2 area led to the detection of a NNW-SSE-oriented ridge that stands out ~ 20 m above the paleorelief of the BM. Bouguer gravity and aeromagnetic data analysis shows that this ridge corresponds the steeply-dipping quartzitic layers of the upper part of the Blanmont Formation, the oldest formation in the Brabant Massif. East of the ridge, the more resistive lower part of the younger Tubize Formation is present.
- The high impedance contrast between the BM and its sedimentary cover and the positive comparison between potential field data and bedrock depth demonstrate that a densely spaced grid of non-invasive HVSR can be successfully used as a tool to study the bedrock paleorelief in Central Belgium.

Acknowledgements Methodology was developed during the BELSPO MO-33-028 and FNRS T.0116.14 projects. The Geological Survey of Belgium provided funding for the 2017 field campaign. M. Deceuckelaire (GSB) is thanked for discussion on borehole data. Volle Gas (Elsene) is sincerely thanked to provide logistics while coding. We thank C. Mascandola and an anonymous reviewer for their valuable comments to improve this work.

Contributions Master thesis of J.M., supervised by K.V.N. and T.L., was at the origin of this work; K.V.N. and T.L. developed python codes for data analysis; K.V.N., B.M., C.G., J.M., and X.D. conducted fieldwork; K.V.N., C.G., and X.D. processed the ambient noise data; K.V.N., T.L., T.D., and X.D. interpreted results; K.V.N. wrote the manuscript in the framework of the Brain.be 2.0 GEOCAMB project (B2/191/P1/GEOCAMB). All authors approved the final manuscript.

Data availability The workflow developed to visualise H/V spectral ratios of ambient noise measurements from Geopsy outputs is available on Github (Van Noten et al., 2020; https://github.com/KoenVanNoten/HVSR_to_virtual_borehole). The Python codes use SciPy (Jones et al. 2001), the Matplotlib library (Hunter 2007) and Numpy (Oliphant 2006). Codes allow (i) creating a database reading the open-source software Geopsy .hv files; (ii) interpolating between resonance frequency and amplitude to improve f_0 picking; (iii) plotting a Virtual Borehole from a *.hv* Geopsy file (Fig. 3) using a power law equation; and (iv) creating a polarisation plot from the rotational HV module Geopsy output file (Fig. 4). Raw ambient noise data are available upon request. The H/V processed data of noise measurements above boreholes and from the case study, their *.hv* Geopsy file analysis, the virtual borehole plots, and the polarisation plots are all available in the Electronic

Supplement. Maps were created using QGIS (QGIS Development Team 2021).

Declarations

Conflict of interest The authors declare no competing interests.

References

Bauer BO, Shermann DJ, Wolcott JF (1992) Sources of uncertainty in shear stress and roughness length estimates derived from velocity profiles. Prof Geogr 44:453–464

Benjumea B, Gabàs A, Bellmunt F, Figueras S, Cirés J (2011) Integrated geophysical profiles and H / V microtremor measurements for subsoil characterization. Near Surface Geophysics 9:413–425

Bignardi S (2017) The uncertainty of estimating the thickness of soft sediments with the HVSR method : a computational point of view on weak lateral variations. J Appl Geophys 145:28–38

Borges JF, Silva HG, Torres RJG, Caldeira B, Bezzeghoud M, Furtado JA, Carvalho J (2016) Inversion of ambient seismic noise HVSR to evaluate velocity and structural models of the Lower Tagus Basin. Portugal J Seism 20:875–887

Buffel, P, Matthijs, J (2009) Kaartblad (31-39) Brussel - Nijvel. Schaal 1:50,000. Toelichtingen bij de geologische kaart van België – Vlaams Gewest. BGD – ANRE / ALBON, vol 31, p 1–53

Cambier G, Devleeschouwer X (2013) A GIS-based methodology for creating 3D geological models in sedimentary environment: application to the subcrop of Brussels. Zeitschrift Der Deutschen Gesellschaft Für Geowissenschaften 164(4):557–567

Cauchie L, Cushing ECG, Froment B, Provost L, Jomard H, Sariguzel B 2017 Site response assessment in two geological contexts, France. SSA 2017 Annual Meeting, 18–20 April 2017. https://doi.org/10.13140/RG.2.2.19493.50401

Chacksfield BC, Vos WD, D'Hooge L, Dusar M, Lee MK, Poitevin C, Royles CP, Verniers J (1993) A new look at Belgian aeromagnetic and gravity data through image-based display and integrated modelling techniques. Geol Mag 130:583–591

Chacksfield BC, Williamson JP Pharaoh TC, McEvroy FM (2004) Reinterpretation of the gravity anomalies over the Brabant Massif in southern Flanders (Belgium), British geological survey commissioned Report, CR/04/215, 47 p

Chatelain J-L, Gueguen P, Guillier B, Frechet J, Bondoux F, Sarrault J, Sulpice P, Neuville J-M (2000) CityShark: a user-friendly instrument dedicated to ambient noise (Microtremor) recording for site and building response studies. Seismol Res Lett 71:698–703

Chatelain J-L, Guillier B, Cara F, Duval AM, Atakan K, Bard PY (2008) Evaluation of the influence of experimental conditions on H/V results from ambient noise recordings. Bull Earthq Eng 6:33–74

Databank Ondergrond Vlaanderen (2020a) G3Dv3, the Geological 3D layermodel of Flanders Vlaanderen and Brussels Capital Region. https://dov.vlaanderen.be/page/geologisch-3d-model-g3d. Accessed 1 Oct 2020

Databank Ondergrond Vlaanderen (2020b) Gravimetrie. https://dov.vlaanderen.be/page/gravimetrie. Accessed 1 Oct 2020

Debacker TN (2001) Palaeozoic deformation of the Brabant Massif within eastern Avalonia: how, when and why? PhD Thesis. Vakgroep Geologie en Bodemkunde. Universiteit Gent, Gent

Debacker TN (2012) Folds and cleavage/fold relationships in the Brabant Massif, southeastern Anglo-Brabant Deformation Belt. Geol Belgica 15:81–95

Debacker TN, Dewaele S, Sintubin M, Verniers J, Muchez P, Boven A (2005) Timing and duration of the progressive deformation of the Brabant Massif. Belgium Geol Belgica 8:20–34

Debacker TN, Sintubin M, Verniers J (2004) Transitional geometries between gently plunging and steeply plunging folds : an example from the Lower Palaeozoic Brabant Massif, Anglo-Brabant deformation. J Geol Soc London 161:1–12

Deckers, J. & Matthijs, J. (2016) Middle Paleocene uplift of the Brabant Massif from central Belgium up to the southeast coast of England. *Geol. Mag.*, 1–10, Cambridge, UK: Cambridge University Press

Delgado J, Alfaro P, Galindo-Zaldivar J, Jabaloy A, López Garrido AC, Sanz de Galdeano C (2002) Structure of the Padul-Nigüelas basin (S Spain) from H/V ratios of ambient noise: application of the method to study peat and coarse sediments. Pure Appl Geophys 159:2733–2749

Devleeschouwer X, Goffin C, Vandaele J, Meyvis B (2017) Brustrati3D Project. Version 1.0. Modélisation stratigraphique en 2D et 3D du sous-sol de la Région de Bruxelles-Capitale, Brussels. Published Final Report, p105. https://environnement.brussels/thematiques/geologie-et-hydrogeologie/geologie. Accessed 9 Jan 2019

Digital Elevation Model Flanders II (2018) Databank Ondergrond Vlaanderen. https://overheid.vlaanderen.be/en/producten-diensten/digital-elevation-model. Accessed 18 Apr 2018

Di Giulio G, G Cultrera C, Cornou P-Y, Bard B Al Tfaily 2019 Deliverable D7.2 - best practice and quality assessment guidelines for site characterization, 75 pages

Dinesh BV, Nair GJ, Prasad AGV, Nakkeeran PV, Radhakrishna MC (2009) Relation between sedimentary layer thickness and fundamental frequency of the H/V spectra for Bangalore city. Curr Sci 97:1973–1977

Everaerts M (2000) *L'interprétation structurale de la Manche au Rhin: apport du filtrage des champs de potentiel*. Unpublished PhD Thesis. Université Catholique de Louvain, Belgium, 167 p

Fäh D, Giardini D, Kind F (2001) A theoretical investigation of average H/V ratios. Geophys J Int 145:535–549

García Moreno D, Camelbeeck T (2013) Comparison of ground motions estimated from prediction equations and from observed damage during the M = 4.6 1983 Liège earthquake (Belgium). Nat Hazards Earth Syst Sci 13:1983–1987

Geological Survey of Belgium (2018) GISEL. Borehole database. http://gisel.naturalsciences.be/gisel/gisel.html. Accessed 12 June 2018

Guéguen P, Cornou C, Garambois S, Banton J (2007) On the limitation of the H/V spectral ratio using seismic noise as an exploration tool: application to the Grenoble Valley (France), a Small Apex Ratio Basin. Pure Appl Geophys 164:115–134

Herbosch A, Debacker TN (2018) A new geological map of the outcrop areas of the Brabant Massif (Belgium). Geol Belgica 21:41–58

Hinzen K-G (2005) Ground motion parameters of the July 22, 2002 ML 4.9 Alsdorf (Germany) earthquake. Boll Di Geofis Teor Ed Appl 46:303–318

Hinzen K-G, Weber B, Scherbaum F (2004) On the resolution of H/V measurements to determine sediment thickness, a case study across a normal fault in the lower rhine embayment. Germany J Earthq Eng 8:909–926

Hollender F, Edward M, Philippe C, Stéphane D, Cédric N, Bailly GT, Delavaud E et al (2015) Evaluation of site effect features of Miocene Paleo-canyons in South Eastern France using ambient vibration methods. SSA, 2015 Annual Meeting 21 – 23 April Pasadena, California CA, USA

Hunter JD (2007) Matplotlib: A 2D graphics environment. Comput Sci Eng 9:90–95

Ibs-von Seht M, Plenefisch T, Klinge K (2008) Earthquake swarms in continental rifts — a comparison of selected cases in America, Africa and Europe. Tectonophysics 452:66–77

Ibs-von Seht M, Wohlenberg J (1999) Microtremor measurements used to map thickness of soft sediments. Bull Seismol Soc Am 89:250–259

Jones E, Oliphant E, Peterson P (2001) SciPy: open source scientific tools for Python, http://www.scipy.org/. Last access: 22 April 2019

Konno K, Omachi T (1998) Ground-motion characteristics estimated from spectral ratio between horizontal and vertical components of microtremor. Bull Seism Soc Am 88:228–241

Legrand L (1968) Le Massif du Brabant. Service Géologique de Belgique. Mémoires pour servir à l'explication des cartes géologiques et minières de la Belgique 9:1–148

Loveless S, Hoes H, Petitclerc E Licour L, Laenen B (2015) Country update for Belgium. *Proc. World Geotherm. Congr. 2015*, Melbourne, Australia, 19–25 April 2015

Macau A, Benjumea B, Gabàs A, Figueras S, Vilà M (2015) The effect of shallow quaternary deposits on the shape of the H/V spectral ratio. Surv Geophys 36:185–208

Mascandola C, Massa M, Lovati S, Augliera P (2018) The site characterization scheme of the INGV Strong Motion Database (ISMD): overview and site classification. Seismol Res Lett 89(1):86–98

Mascandola C, Massa M, Barani S, Albarello D, Lovati S, Martelli L, Poggi V (2019) Mapping the seismic bedrock of the Po Plain (Italy) through ambient-vibration monitoring. Bulletin of the Seismological Society of America 109(1):164–177

Massa M, Lovati S, D'Alema E, Ferretti G, Bakavoli M (2010) An experimental approach for estimating seismic amplification effects at the top of a ridge, and the implication for ground-motion predictions: the case of Narni, Central Italy. Bull Seism Soc Am 100:286–301

Matsushima S, Hirokawa T, De Martin F, Kawase H, Sánchez-Sesma FJ (2014) The effect of lateral heterogeneity on horizontal-to-vertical spectral ratio of microtremors inferred from observation and synthetics. Bull Seis Soc Am 104:381–393

Matthijs J, Debacker TN, Piesens K, Sintubin M (2005) Anomalous topography of the lower Palaeozoic basement in the Brussels region. Belgium Geol Belgica 8:69–77

Molron J (2015) Thickness estimation of sediments overlying the Brabant Massif by H/V spectral ratio analysis in central Belgium. Université libre de Bruxelles. M.Sc, Thesis

Nakamura Y (1989) A method for dynamic characteristics estimation of subsurface using microtremor of the ground surface. QR RTR I:30

Nguyen F, Rompaey GV, Teerlynck H, Camp MV, Jongmans D (2004) Use of microtremor measurement for assessing site effects in Northern Belgium – interpretation of the observed intensity during the Ms = 5.0 June 11 1938 earthquake. J Seismol 8:41–56

Nogoshi M, Igarashi T (1970) On the propagation characteristics of microtremors. Zisin 23:264–280

Oliphant, T.E. (2006) A guide to NumPy, USA: Trelgol Publishing. http://www.numpy.org. Last access: 15 March 2019

Paratore M, Zuccarello L, Tusa G, Contrafatto D, Patanè D (2013) Seismic amplification effects and soil-to-structure interaction study nearby a fault zone: the Tremestieri Fault and Madre Teresa Di Calcutta School (Catania). Ann Geophys 61:SE226

Parolai S, Bormann P, Milkert C (2002) New relationships between Vs, thickness of sediments, and resonance frequency calculated by the H/V ratio of seismic noise for Cologne Area (Germany). Bull Seis Soc Am 92:2521–2527

Peeters L, Fasbender D, Batelaan O, Dassargues A (2010) Bayesian data fusion for water table interpolation: incorporating a hydrogeological conceptual model in kriging. Water Resour Res 46:W08532

Pedersen H, Brun BL, Hatzfeld D, Campillo M, Bard PY (1994) Ground-motion amplitude across ridges. Bull Seismol Soc Am 84:1786–1800

Petermans T, Devleeschouwer X, Pouriel F, Rosset P (2006) Mapping the local seismic hazard in the urban area of Brussels, Belgium. 10th IAEG Congress "Engineering geology for tomorrow's cities". Paper number 424. 11p

Petitclerc E, Welkenhuysen K, Passel SV, Piessens K, Maes D, Compernolle T (2017) Towards geological-economic modelling to improve evaluating policy instruments for geothermal energy – case study for Belgium (Campine Basin). Eur Geol J 43:10–15

Piessens K, Vos W, De Herbosch A, Debacker TN, Verniers J (2004) Lithostratigraphy and geological structure of the Cambrian rocks at Halle-Lembeek (Senne Valley, Belgium). Geological Survey of Belgium - Professional Paper 300:1–142

Poggi V, Fäh D, Burjanek J, Giardini D (2012) The use of Rayleigh-wave ellipticity for site-specific hazard assessment and microzonation: application to the city of Lucerne. Switzerland Geophys J Int 188:1154–1172

QGIS Development Team (2021) QGIS Geographic Information System. Open Source Geospatial Foundation. http://qgis.osgeo.org. Last access: 1 July 2021

Roesset JM (1970) Fundamentals of soil amplification, in Seismic Design for Nuclear Power Plants. in *Seismic Design for Nuclear Power Plants* ed. Hansen, R.J., pp. 183–244, Cambridge, MA.: M.I.T. Press

Rosset P, Petermans T, Devleeschouwer X, Pouriel F, Camelbeeck T (2005) Identifying the influence of the local geology in case of earthquake for urban planning: case study in Brussels. *Les journées Géographiques Belges, Mobilité, Société Environ. en Cart*., novembre 2005, T.II, 171–177

SESAME (2005) Guidelines for the implementation of the H/V spectral ratio technique on ambient vibrations - measurements, processing and interpretations. SESAME Eur Res Proj Deliv D23(12):2005

Sintubin M (1999) Arcuate fold and cleavage patterns in the southeastern part of the Anglo-Brabant fold Belt (Belgium): tectonic implications. Tectonophysics 309:81–97

Sintubin M, Brodkom F, Laduron D (1998) Cleavage-fold relationship in the Lower Cambrian Tubize Group, southeast Anglo-Brabant Fold Belt. Geol Mag 135:217–226

Thabet M (2019) Site-specific relationships between bedrock depth and HVSR fundamental resonance frequency using KiK-NET data from Japan. Pure Appl Geophys 176:4809–4831

van Ginkel J, Ruigrok E, Herber R (2020) Using horizontal to vertical spectral ratios to construct shear-wave velocity profiles. Solid Earth Discuss. 1–28. 10.5194/se-2020-86

Van Noten K, Lecocq T, Shah AK, Camelbeeck T (2015a) Seismotectonic significance of the 2008–2010 Walloon Brabant seismic swarm in the Brabant Massif, Belgium. Tectonophysics 656:20–38

Van Noten K, Lecocq T, Camelbeeck T (2015b) The seismic activity in the Walloon Brabant and its relationship with the local and regional geological structure. Final report of Belgian Science Policy contract MO/33/028. Royal Observatory of Belgium. p79. https://doi.org/10.13140/RG.2.2.12302.87364

Van Noten K, Lecocq T, Sira C, Hinzen KG, Camelbeeck T (2017) Path and site effects deduced from merged transfrontier internet macroseismic data of two recent M4 earthquakes in northwest Europe using a grid cell approach. Solid Earth 8:453–477

Van Noten K, Lecocq T, Power B (2020) HVSR to virtual borehole (Version 1.0). Zenodo. https://doi.org/10.5281/zenodo.4276310

Verbeeck (2019) Deterministic seismic hazard assessment in the Belgian Campine basin at the Mol/Dessel site: From seismic source to site effect. Unpublished PhD thesis. KULeuven. 398p

Wathelet M, Chatelain J-L, Cornou C, Di Giulio G, Guillier B, Ohrnberger M, Savvaidis A (2020) Geopsy: a user-friendly open-source tool set for ambient vibration processing. Seismol Res Lett 91:1878–1889

Williamson JP, Chacksfield BC, Pharaoh TC, McEvoy FM (2004) Reinterpretation of gravity anomalies over the Brabant Massif in southern Flanders (Belgium). British Geological Survey Commissioned Report, CR/04/215, 47p